# Ophthalmic magnetic resonance imaging at 7.0 T using a 6-channel transceiver radiofrequency coil array in healthy subjects and patients with intraocular masses

*Graessl, A., Muhle, M., Schwerter, M., Rieger, J., Oezerdem, C., Santoro, D., Lysiak, D., Winter, L., Hezel, F., Waiczies, S., Guthoff, R.F., Falke, K., Hosten, N., Hadlich, S., Krueger, P.C., Langner, S., Stachs, O., Niendorf, T.*

This is a non-final version of an article published in final form in:
Investigative Radiology. 2014 May; 49(5): 260-270 | doi: 10.1097/RLI.0000000000000049
Lippincott Williams & Wilkins (U.S.A.) ►

# Ophthalmic MRI at 7.0 Tesla Using a Six-Channel Transceiver Radiofrequency Coil Array in Healthy Subjects and Patients with Intraocular Masses

## Abstract

### Objectives

This study is designed to examine the feasibility of ophthalmic MRI at 7.0 T using a local six-channel transmit/receive radiofrequency (RF) coil array in healthy volunteers and patients with intraocular masses.

### Materials and Methods

A novel six-element transceiver RF coil array that makes uses of loop elements and that is customized for eye imaging at 7.0 T is proposed. Considerations influencing the RF coil design and the characteristics of the proposed RF coil array are presented. Numerical electro-magnetic field (EMF) simulations were conducted to enhance the RF coil characteristics. Specific absorption rate (SAR) simulations and a thorough assessment of RF power deposition were performed to meet the safety requirements. Phantom experiments were carried out to validate the EMF simulations and to assess the real performance of the proposed transceiver array. Certified approval for clinical studies was provided by a local notified body prior to the *in vivo* studies. The suitability of the RF coil to image the human eye, optical nerve and orbit was examined in an *in vivo* feasibility study including (i) 3D gradient echo imaging (3D GRE), (ii) inversion recovery 3D gradient echo (3D IR-GRE) and (iii) 2D $T_2$ weighted fast spin-echo (2D FSE) imaging. For this purpose healthy adult volunteers (n=17, mean age 34±11 years) and patients with intraocular masses (uveal melanoma, n=5, mean age 57±6years) were investigated.

### Results

All subjects tolerated all examinations well with no relevant adverse events. The six-channel coil array supports high resolution 3D GRE imaging with a spatial resolution as good as (0.2 x 0.2 x 1.0) $mm^3$ which facilitates the depiction of anatomical details of the eye. Rather uniform signal intensity across the eye was found. A mean signal-to-noise ratio (SNR) of approximately 35 was found for the lens while the vitreous humor showed an SNR of

approximately 30. The lens-vitreous humor contrast-to-noise ratio was 8, which allows good differentiation between the lens and the vitreous compartment. Inversion recovery prepared 3D GRE using a spatial resolution of (0.4 x 0.4 x 1.0 mm)$^3$ was found to be feasible. $T_2$-weighted 2D FSE imaging with the proposed RF coil afforded a spatial resolution of (0.25 x 0.25 x 0.7 mm)$^3$.

**Conclusions**

This work provides valuable information on the feasibility of ophthalmic MRI at 7.0 T using a dedicated six-channel transceiver coil array that supports the acquisition of high contrast, high spatial resolution images in healthy volunteers and patients with intraocular masses. The results underscore the challenges of ocular imaging at 7.0 T and demonstrate that these issues can be offset by using tailored RF coil hardware. The benefits of such improvements would be in positive alignment with explorations that are designed to examine the potential of MRI for the assessment of spatial arrangements of the eye segments and their masses with the ultimate goal to provide imaging means for guiding treatment decisions in ophthalmological diseases.

**Key words:** ultrahigh field; magnetic resonance; ophthalmic imaging; intraocular mass; RF coil technology

## Introduction

Magnetic resonance imaging (MRI) of the spatial arrangements of the eye segments and their masses is an emerging MRI application [1-9]. Ocular MRI holds the potential to provide guidance during diagnostic assessment and treatment of ophthalmological diseases [8, 10-13]. With a sensitivity that is close to that of CT, MRI can serve as a diagnostic tool for eye tumors as well as optic neuropathies such as optic neuritis [14-20]. Ultimately, the development of ocular MRI applications is aiming at MR image based biometry [21, 22] to support advanced intraocular lens implantation or refilling procedures that restore visual function and accommodation [23]. These efforts include research into the quantification of age-related and accommodative induced changes in ocular dimensions *in vivo* [24, 25].

MRI of subtle ocular structures requires a sub-millimeter spatial resolution over a small field of view (FOV) [26]. Realizing this constraint as well as the opportunities given by the signal-to-noise ratio (SNR) gain inherent to ultrahigh field (UHF) MRI – which can be translated into spatial resolution enhancements - it is conceptually appealing to pursue *in vivo* MRI of the human eye at high and ultrahigh ($B_0 \geq 7.0$ T) magnetic field strengths [27, 28].

Recognizing the challenges and opportunities of UHF-MR this study examines the feasibility of ophthalmic MRI at 7.0 T. To meet this goal we propose a six-element transceiver RF coil array that covers both eyes (3 elements per eye), that is customized for eye imaging at 7.0 T and that provides image quality suitable for *in vivo* use together with patient comfort and ease of use. For this purpose considerations influencing the RF coil design and the characteristics of the proposed RF coil array are presented in conjunction with numerical electro-magnetic field (EMF) simulations. To meet the safety and RF power deposition limit requirements of MRI, specific absorption rate simulations are conducted. Phantom experiments are performed to validate the EMF simulations and to carefully assess the performance of the proposed transceiver array. Prior to the *in vivo* studies a certification procedure is performed followed by certified approval for clinical studies provided by a notified body. The RF coil's suitability for imaging the human eye, optical nerve, ocular muscles and orbit is examined in an initial feasibility study including healthy adult volunteers and patients with intraocular masses (uveal melanoma). The merits and limitations of the

proposed transceiver array are discussed and implications for clinical ophthalmic MRI at 7.0 T are considered.

## Material and Methods

### *RF Coil Design*

To balance the competing constraints of element size, number of elements, anatomical coverage, RF depth penetration, $B_1^+$ efficiency and parallel imaging performance a symmetric six channel RF coil design (f=298 MHz) with three planar transceiver loop elements per eye was developed as illustrated in Figure 1a. The three loop elements are angled to each other to conform to the anterior head as demonstrated in Figure 1a and 1b. An inclination angle of 151° is used for the arrangement of element 1 (or element 6) vs. element 2 (or element 5). For the arrangement of element 2 (or element 5) vs. element 3 (or element 4) an angle of 161° was applied. The dimensions and size of the individual elements were chosen to balance anatomic coverage with the number of elements (Figure 1c). For this purpose electromagnetic field (EMF) simulations and preliminary workbench tests were conducted. For elements 1, 2, 5 and 6 a rectangular shape was used. For elements 3 and 4 a polygonal shape was employed to allow space for the nose. The width of the elements was set to 36 mm to provide sufficient RF depth penetration within the region of interest (ROI). An element height of 71 mm was used. The structure shown in Figure 1c was etched from 16 µm copper on 0.5 mm FR4 substrate. Together with a conductor width of 10mm this manufacturing procedure assures reproducibility of the coil configuration in the simulation model. For adjacent element decoupling a common conductor with a non-magnetic trimmer capacitor (Voltronics Inc., Denville, NJ, USA) was used as shown in Figure 1b. Next neighbor decoupling was achieved using coaxial cables and two trimmer capacitors that were placed externally to the array [29] as illustrated in Figure 1c. All other elements were decoupled by distance. An RF shield was not implemented since it would prohibit vision through the coil.

Non-magnetic ceramic capacitors (American Technical Ceramics Inc., Huntington Station, NY, USA) and non-magnetic trimmer capacitors (Voltronics Inc., Denville, NJ, USA) were used for tuning, matching and subdividing the conductor loops into short sections. Unbalanced currents on the coaxial cables were suppressed by one cable trap per channel.

Cable traps were designed as double-turn solenoids of the coaxial cable with an appropriate capacitor soldered to the outer conductor at the crossing of the cable. With this parallel resonant circuit an effective reduction of shield currents at 297 MHz is achieved.

The RF coil was built in our laboratory and was not provided by a vendor. The RF coil casing shown in Figure 2 was designed in Autodesk Inventor Professional 2012 (Autodesk Inc., San Rafael, CA, USA). The coil casing was made from ABS+ material using a rapid prototyping system (BST 1200es, Dimension Inc., Eden Prairie, MN, USA). The coil casing accommodates the loop elements, the decoupling networks as well as the cable traps as demonstrated in Figure 2. The housing ensures a minimum distance of 12 mm from the current-carrying conductors to the subject's tissue. The basic geometry of the casing resembles that of a pair of glasses including a soft nose piece. This approach provides means for fitting the coil securely on the bridge of the nose and along the cheek bones. An adjustable, washable head strap helps to hold the RF coil in place. The loop areas of element 3 and 4 are in alignment with the eyes for maximum vision through the RF coil's casing, an approach which has been implemented for eye fixation reasons.

***Numerical Electromagnetic Field Simulations***

Three dimensional electromagnetic field simulations were conducted using the Finite Integration Technique (CST Studio Suite 2011, CST AG, Darmstadt, Germany). For EMF simulations a virtual model of the RF coil configuration - which resembles the experimental version - was used together with the human voxel models 'Duke' and 'Ella' from the Virtual Family (IT'IS Foundation, Zuerich, Switzerland) and with a cylindrical phantom (radius = 60 mm, length = 250 mm, setup with a dielectric with $\varepsilon_r$ = 57.8 and $\sigma$ = 0.78 S/m) [30]. An isotropic resolution of 1.2 mm was used to establish a uniform mesh across the calculation volume. This mesh was locally refined in the area of the conductors, the eyes and the brain. Decoupling capacitors were incorporated in the EMF simulations as lumped elements and they were iteratively adjusted. The feeding points of the elements were modeled as 50 Ω ports. Final field results were accomplished incorporating lumped tuning and matching capacitors in the built-in circuit simulator of CST Studio Suite (CST Design Studio), following a previously

proposed workflow [31]. The capacitor values were optimized with respect to the S-parameter simulation and were used as a starting point for the practical realization. Using the results of the EMF simulations the SAR values were calculated for the final configuration and for phase settings used in *in vivo* measurements. The input power was adjusted to meet the regulations of the IEC guideline IEC 60601-2-33 Ed.3 [32].

***Bench Evaluation of RF Coil Performance***

Bench measurements and characterization of the RF key performance parameters were performed using an 8-channel vector network analyzer (ZVT 8, Rohde & Schwarz, Memmingen, Germany). Measurements of the full set of scattering parameters (S-parameter) were conducted simultaneously for all channel combinations in a frequency range of (250-350) MHz. using a phantom and 6 volunteers (5 male, 1 female, BMI 21-25) to cover various coil loading conditions.

***Magnetic Resonance Hardware***

MR experiments were conducted on a 7.0 T whole body system (Magnetom, Siemens Healthcare, Erlangen, Germany), equipped with an Avanto gradient system (slew rate: 200 mT/m/ms, maximum gradient strength: 45 mT/m; Siemens Medical Solutions, Erlangen, Germany) and an 8 kW single channel RF amplifier (Stolberg HF-Technik AG, Stolberg-Vicht, Germany). The RF signal was split from 1 to 6 signals by means of home-built power splitters. For this purpose Wilkinson power splitters were used in lumped element design that features equal amplitude and zero phase outputs. All 6 elements were connected to the system through a multipurpose interface box equipped with transmit/receive switches and integrated low-noise preamplifiers (Stark Contrasts, Erlangen, Germany). Phase adjustment of each channel was accomplished by adding coaxial cables with the appropriate length to the power splitting network. For comparison, coil configurations (Nova Medical, Wilmington, MA, USA) tailored for head imaging at 7.0 T were employed. The head coil configurations are equipped with a quadrature coil used for transmission which is incorporated in a helmet that closely fits to the head. One configuration accommodates 24 receive elements (1TX24RX).

Another configuration comprises 32 receive elements (1TX32RX) and has elements which encircle the eyes. While these are fairly large elements not optimized for ocular imaging, they do provide much better sensitivity over the eyes than with the 1TX24RX configuration. For the 1TX1RX configuration the quadrature volume coil was used for transmission and for reception.

**Transmission Field Shimming**

The right eye was selected first for transmission field ($B_1^+$) shimming since the imaging sessions were designed to include only one eye per examination due to the setup used for reduction of eye motion artifacts. The results derived from EMF simulations of the elements 1, 2 and 3 were extracted and a nonlinear optimization algorithm was used in Matlab (The MathWorks, Inc., Natick, MA, USA) to homogenize the resulting $B_1^+$ field. The resulting transmission field was calculated by superimposing the field of each channel with different phase. The merit function for the $B_1^+$ shimming was dynamically updated to a constant field strength, equivalent to the median value of the intermediate result. The phase settings obtained for the right eye were ported to the left eye. This approach provided a similar $B_1^+$ field distribution for the right and for the left eye. In the experiment, an element-wise $B_1^+$ shimming was performed by incorporating coaxial cables for each loop element into the power splitting network.

***Phantom Experiments***

For validation of the $B_1^+$ shimming results derived from the simulations, phantom studies were performed. Simulated absolute $B_1^+$ distributions of the individual coil elements were compared with maps of absolute $B_1^+$ fields derived from measurements. For this purpose the RF coil was placed on a cylindrical phantom (Figure 2). The phantom (radius = 60 mm, length = 250 mm) was filled with a dielectric gel ($\varepsilon_r$ = 57.8, $\sigma$ = 0.78 S/m) to resemble the setup used for EMF simulations in order to compare results from simulations with those from phantom experiments. RF transmission field mapping was conducted using the ΦFA CUP approach [33, 34] in conjunction with a 3D GRE imaging module. For this purpose a rectangular composite pulse of 400µsec, a total flip angle=150°, TR= 100ms, matrix 64x64x20, acquisition time per channel=256 s were used. A transmitter reference voltage=50 Volt was applied resulting in a

nominal $B_1^+$=19.16 µT with an RF duty cycle of 0.4%. The sequence employed double gradient echo acquisitions to enable static magnetic field ($B_0$) mapping [35] with echo times of TE1=1.6 ms and TE2=4.1 ms. Volume selective second order $B_0$ shimming was performed and $B_0$ non-uniformities were accounted for in a post-processing routine. All absolute values were normalized to the input power at the feeding point of the loop structure.

***Ethics Statement***

For the *in vivo* feasibility study, subjects were included after due approval by the local ethical committee (registration number DE/CA73/5550/09, Landesamt für Arbeitsschutz, Gesundheitsschutz und technische Sicherheit, Berlin, Germany). Informed written consent was obtained from each volunteer and patient prior to the study in compliance with the local institutional review board guidelines.

***Volunteer and Patient Study***

Prior to the volunteer study the RF coil underwent thorough safety assessment in line with IEC 60601-2-33:2010 Ed.3 and IEC 60601-1:2005 Ed.3 [32]. The safety assessment, the implemented safety measures, the technical documentation and the risk management file for the coil were evaluated and duly approved for implementation in clinical studies following certification by the notified body.

MR imaging was performed in healthy adult volunteers (n=17, mean age 34±11 years, range 24-64 years, BMI 24.5±2,) and in patients with intraocular masses (uveal melanoma, n=5, mean age 57±6years, range 50-68 years, BMI 26±5).

Absolute transmission field mapping using a Bloch-Siegert implementation [36] was used for flip angle calibration so that the actual flip angle represents the nominal flip angle in the center of the eye.

The imaging protocol included:

- 3D gradient echo imaging (3D GRE) using a linear, regular density Cartesian phase encoding scheme:

a) For a spatial resolution of (0.3 x 0.3 x 1.0) $mm^3$ the parameters were: TR=10.3 ms, TE=3.6 ms, nominal flip angle 6°, FOV=(81 x 58) $mm^2$, matrix size=320 x 230, 24 slices per slab, receiver bandwidth of 300 Hz/pixel, number of averages=2. The nominal acquisition time was 3:12 min.

b) For a spatial resolution of (0.2 x 0.2 x 1.0) $mm^3$ the parameters were: TR = 12 ms, TE = 5.9 ms, nominal flip angle 8°, FOV = (50 x 50) $mm^2$, matrix size = 256 x 256, 32 slices per slab, receiver bandwidth of 230 Hz/pixel. The acquisition time was 2:09 min including resting periods for eye blinking.

- Inversion recovery 3D gradient echo (3D IR-GRE) with a spatial resolution of (0.4 x 0.4 x 1.0) $mm^3$, TR = 13.6 ms, TE = 6.5 ms, inversion time TI= 1900 ms, nominal flip angle 6°, FOV = (103 x 74) $mm^2$, matrix size = 256 x 184, 24 slices per slab, receiver bandwidth=300 Hz/pixel, 2 averages, and linear, regular density Cartesian phase encoding. The nominal acquisition time was 1:43 min.
- 2D $T_2$ weighted fast spin-echo (2D FSE) imaging using a spatial resolution of (0.25 x 0.25 x 0.7) $mm^3$, TR=2940 ms, TE=85 ms, nominal flip angle of the refocussing pulses= 100°, FOV = (84 x 60) $mm^2$, matrix size = 384 x 245, 6 slices, receiver bandwidth of 260 Hz/pixel, 4 averages, and two-fold acceleration along the A-P phase encoding direction using GRAPPA reconstruction. The acquisition time was approximately 2:00 min per average including resting periods for eye blinking.

For comparison, $T_2$-weighted 2D FSE imaging was performed using the 1TX24RX, 1TX1RX, 1TX32RX head coil configurations. For this purpose the imaging parameters were adjusted to avoid folding artifacts:

- 1TX24RX: TR=2940 ms, TE=85 ms, spatial resolution=(0.53 x 0.53 x 0.7) $mm^3$, FOV=(204 x 130) $mm^2$, matrix size=384 x 245, receiver bandwidth=260 Hz/pixel, 4 averages, acquisition time=2:00 min per average and two-fold acceleration along the A-P phase encoding direction using GRAPPA reconstruction.
- 1TX1RX: TR=2940 ms, TE=72 ms, spatial resolution = (0.52 x 0.52 x 1.4) $mm^3$, FOV = (200 x 200) $mm^2$, matrix size=384 x 384, receiver bandwidth =260 Hz/pixel, acquisition time=2:41 min.

- 1TX32RX: TR=2940 ms, TE=72 ms, spatial resolution of (0.52 x 0.81 x 1.4) $mm^3$, FOV = (200 x 200) $mm^2$, matrix size=384 x 246, receiver bandwidth =260 Hz/pixel, acquisition time=2:41 min. Images were re-reconstructed with the scaling factors of all except the three elements closest to the eye set to zero. This gives the equivalent of only receiving on the nearest elements, similar to the proposed 6 channel eye coil setup.

To reduce eye movement artifacts, subjects were prepared as previously described [28]. The investigated eye was kept closed. The contralateral eye was anesthetized (Proparakain-POS 5%, Ursapham, Germany) and lubricated (Thealoz®, Thea Pharma, France). All protocols included a triggering scheme, which consisted of an acquisition window followed by a pause to allow for blinking [28, 36]. The subjects were asked to fixate the gaze of the open eye for 3 s on a far point, which was marked inside the iso-center of the scanner bore. The fixation period was followed by a rest period of 3 s that allowed for blinking. Subsequently, re-fixation was conducted. MR data acquisition was interrupted during the rest periods. The alternating gaze fixation-resting periods were repeated until the end of each scan series.

As part of our standard protocol all subjects were given an exit interview regarding their experience during the 7T examination.

*In vivo* image quality was assessed by determining signal-to-noise ratio (SNR), lens/vitreous humor contrast-to-noise ratio (CNR) and signal intensity uniformity across the lens or the vitreous humor. For SNR and CNR measurements images derived from regularly sampled acquisitions were used. Regions of interest covering the lens or the vitreous humor were used to determine the mean value of the signal intensity. Noise was obtained from the standard deviation of the signal intensity of a ROI positioned well outside of the head. Geometry factors (g-factor) were determined as previously described [37].

## Results

### *RF Characteristics and Coil Performance*

The RF coil exhibits a weight of m=804 g (versus m=200 g obtained for a single element receive only surface coil (d=60 mm)). Please note that the latter does not include the TR/RX switches and the preamplifier circuit boards which were used for the eye coil) and conforms to a broad range of head and nose geometries, leading to well perceived patient comfort and ease of use. The S-parameter matrices were averaged over five male and one female volunteer. Reflection coefficients of the individual elements averaged over five volunteers ranged between -23 dB and -28 dB (Figure 3A). Element coupling was below -11.4 dB for all elements and subjects. The loop elements were found to have an average $Q_U/Q_L$ of 5.07 (elements 1 and 6), 6.09 (elements 2 and 5) and 2.72 (elements 3 and 4). Noise correlation was examined as previously described [37] and yielded a noise correlation of 0.4 or below for all elements and subjects as shown in Figure 3.

### *Numerical EMF Simulations and SAR Considerations*

The phase optimization algorithm used to tailor $B_1^+$ uniformity yielded a phase setting of Ch1: 0°, Ch2: -327.2°, Ch3: -248°, Ch4: 0°, Ch5: -327.2°, Ch6: -248° (designated as phase setting PS3, negative phase values indicate a phase delay) shown in Figure 4e. For comparison, two circular polarized (CP) phase settings (PS1, PS2) were employed. PS1 represents a CP mode derived from the angles between the loop plane normal vectors (PS1: Ch1: 0°, Ch2: -331°, Ch3: -312°, Ch4: -262°, Ch5: -243°, Ch6: -214°) and provided a $B_1^+$ distribution shown in Figure 4c. To generate a CP mode centered in the left (elements 4,5,6) and in the right eye (elements 1,2,3) PS2 was set to Ch1: 0°, Ch2: -308°, Ch3: -255°, Ch4: -0°, Ch5: -307°, Ch6: $-259^0$ which yielded the $B_1^+$ distribution depicted in Figure 4d. Figure 4f demonstrates improvements in $B_1^+$ uniformity for regions covering the eyes for PS3 versus PS2. For all three phase settings the input power amplitude was equal for each channel.

Local SAR values averaged over 10g ($SAR_{10g}$) were derived from the EMF simulations for PS3 using the human voxel models "Duke" and "Ella" for an accepted input power of 1 W

averaged over a period of 6 min. Subsequently the maximum input power was limited to 0.8 W to ensure that the $SAR_{10g}$ maxima did not exceed 10 W/kg as demonstrated in Figure 5. The local SAR maxima for PS3 did not even exceed 6.7 W/kg which is well below the limits permitted by the IEC guidelines [32]. The locations and amplitudes of the local maxima are comparable for the voxel models "Duke" and "Ella" as shown in Figure 5.

For the calculation of the head SAR the mass of the head was set to 4.8 kg which corresponds to an average adult head. The 0.8 W input power yielded 0.17 W/kg of head SAR that was below the limit of 3.2 W/kg permitted by the IEC guidelines [32]. The losses in the transmit chain were not included or compensated for in the SAR calculations, therefore a reasonable safety margin is maintained in the maximum input power estimation.

***Validation in Phantom Experiments and $B_1^+$ Mapping***

For all individual elements and for the combination of all elements, the transmission fields obtained from EMF simulations when placed on the virtual cylindrical phantom were found to be in agreement with the $B_1^+$ fields derived from $B_1^+$ mapping in phantom experiments (Figure 6). This supports the validity of the EMF simulations, which is of importance for the SAR assessment.

***In Vivo Feasibility Study***

All volunteers and all patients involved in this study tolerated all examinations well with no relevant adverse events. *In vivo* scout imaging using relatively low spatial resolution imaging revealed rather uniform signal intensity for sagittal and transversal views of the eye. For parallel imaging using 2D FGRE and GRAPPA reconstruction, mean geometry factors of g=1.1 (R=2), g=1.9 (R=3) and g=3.4 (R=4) were determined for a ROI covering the human eye, orbit and segments of the optic nerve.

The *in vivo* feasibility study yielded that the proposed six-channel coil array supports high spatial resolution imaging of the human eye at 7.0 T within clinically acceptable scan times for each protocol resulting in a total examination time of less than 25 min. Figure 7 shows a sagittal view of the eye of a healthy subject derived from 3D gradient echo imaging.

With a spatial resolution of (0.3 x 0.3 x 1.0) $mm^3$ we could clearly discern anatomical details of the eye including the anterior chamber, posterior chamber, lens nucleus, lens cortex, vitreous humor and orbital muscles (Figure 7a). Rather uniform signal intensity was observed across the eye as underlined by the signal intensity profiles through a sagittal view of the lens nucleus and the vitreous humor (Figure 7b). Across the short axis of the lens a 7% change in signal intensity was observed. The mean signal intensity of the lens was found to be 1050±100 with a mean signal-to-noise ratio of approximately 35. The vitreous humor provided a mean signal intensity of 720±50 and a mean SNR of approximately 30. Along a line connecting the center of the lens with the retina a signal intensity change of 15% was observed within the vitreous humor. For a profile perpendicular to the line connecting the lens with the retina a signal intensity change of 2% was determined. The lens-vitreous humor contrast-to-noise ratio was 8, which allows good differentiation between the lens and the vitreous compartment.

Figure 8 demonstrates the feasibility of high spatial resolution 3D GRE imaging. For this purpose transversal views of the eye were acquired using a spatial resolution of (0.2 x 0.2 x 1.0) $mm^3$ (Figure 8a) and of (0.3 x 0.3 x 1.0) $mm^3$ (Figure 8b). We could also demonstrate the feasibility of inversion recovery prepared 3D GRE using a spatial resolution of (0.4 x 0.4 x 1.0 $mm)^3$ (Figure 8c) and $T_2$-weighted 2D FSE with a spatial resolution of (0.25 x 0.25 x 0.7 $mm)^3$ (Figure 8d). For comparison, the $T_2$-weighted 2D FSE protocol was performed using the 1TX24RX, 1TX1RX and 1TX32RX head coil configurations. Figure 9 shows a sagittal view of the eye of healthy subjects derived from 2D FSE acquisitions using the 1TX24RX configuration (Figure 9 a, e), the 1TX1RX configuration (Figure 9b,f), the 1TX32RX configuration (Figure 9c,g) and the 6 channel TX/RX coil (Figure 9 d, h). For the 6 channel TX/RX coil, rather uniform signal intensity was observed across the eye as illustrated in Figure 9m. For a profile perpendicular to the line connecting the lens with the retina a mean signal intensity change of <5 % was determined. In comparison, the 1TX24RX configuration showed a 90 % signal intensity decrease for the same profile as outlined in Figure 9i. When using the 1TX1RX and 1TX32RX configurations a mean signal intensity decrease of approximately 55 % was observed for a profile perpendicular to the line connecting the lens with the retina (Figure 9k,l).

We next wanted to study the applicability of the proposed six-channel coil in patients with ocular tumor masses. Using a spatial resolution of (0.3 x 0.3 x 1.0) $mm^3$, tumor mass and retinal detachment within the eye of patients suffering from melanoma of the choroid membrane can be clearly depicted in both sagittal (Figure 10a) and transversal views (Figure 10b). For comparison, the sagittal view is also shown for an image using an enhanced spatial resolution of (0.2 x 0.2 x 1.0) $mm^3$ (Figure 10c). The retinal detachment of a malignant melanoma of choroidea is also clearly depicted by 2D $T_2$-weighted fast spin-echo imaging using a spatial resolution of (0.25 x 0.25 x 0.7) $mm^3$ (Figure 10e).

## Discussion

This study demonstrates the feasibility of ocular imaging at 7.0 T using a dedicated six-channel transceiver coil array that uses loop elements and that provides image quality and suitability for clinical use, patient comfort and ease of use. The results derived from RF characteristics and noise correlation assessment are encouraging and suggest that subject-specific tuning and matching may not be essential when using the proposed coil array in a clinical setting.

The benefits of the sensitivity gain inherent to UHF-MR together with the SNR gain of the proposed local 6 channel TX/RX coil array – that in contrast to a volume head coil closely fits to the anatomy of the cheek, eyebrow and nose – were exploited for high spatial resolution ophthalmic imaging. Our results demonstrate that the proposed coil design affords uniform signal intensity across a region of interest encompassing the eye and facilitates the depiction of subtle anatomical details of the eye. Our *in vivo* feasibility study using the proposed six-channel array together with a 2D gradient echo imaging protocol yielded a 2% signal intensity change for the vitreous humor along a profile perpendicular to the line connecting the lens with the retina. Along a line connecting the center of the lens with the retina a 15% change in signal intensity was observed across the vitreous humor. In comparison, a pioneering study at 7.0 T employing a volume head coil for transmission and a single element loop coil (diameter= 4cm) for reception reported a signal decay of more than 50% along the same profile through the vitreous humor [28]. For the lens nucleus we observed a signal intensity variation of less than 10 %. In comparison, the single element loop RX coil study reported a signal decay of approximately 25% along the short main axis of the lens nucleus [28]. Rather uniform signal intensity across the eye was also observed for 2D-weighted FSE imaging. For this protocol a mean signal intensity change of <5 % was obtained for a profile perpendicular to the line connecting the lens with the retina. Further to ocular imaging the coil might be also suitable for targeting deeper lying sections of the orbit, the optical canal and the optic nerve. Anatomical imaging of the optic nerve bears clinical relevance for optic neuropathies in neuroinflammatory diseases and also for the differential diagnosis of debilitating autoimmune or orphan diseases of the central nervous system that run the risk of

visual impairment [38, 39]. Adding a support structure to the coil that still supports a close fit to the cheekbones and the forehead would render the coil effectively weightless for the subject.

A recent study examined the diagnostic value of ophthalmic MRI at 1.5 T using an in-plane spatial resolution ranging from (0.31-0.62) mm in conjunction with a slice thickness ranging from (1.6-4.0) mm [40]. The same study concluded that further technological advancements in the field are required to provide more spatially detailed images of the eye, the structures in the orbit and the optic nerve [40]. This conclusion prompted the authors to propose the use of highfield MR systems in conjunction with surface coils. Our study adds to the literature by demonstrating the feasibility of ophthalmic MRI at 7.0 T using a spatial resolution as good as (0.2 x 0.2 x 1.0) $mm^3$. Unlike previous studies we did not use general anesthesia for high spatial resolution imaging of the eye [40].

The proposed coil array yielded a mean geometry factor of $g<2$ for a 1D acceleration factor of R=3. It is perceivable that the maximum possible acceleration increases with increasing number of array elements; an approach which needs to be carefully balanced with the competing constraints of coil element size, RF depth penetration and eye coverage. Recognition of the benefits and performance of multi-dimensional local surface coil arrays might be translated into reduction of noise amplification inherent in parallel imaging with the goal to preserve SNR versus one-dimensional accelerations [41-45]. This would require a two-dimensional array tailored for ocular imaging with loop elements with a diameter or element height substantially smaller than the h=71 mm used in this study.

Imaging a relatively small field of view is another challenge of ophthalmic MRI since it bears the risk of aliasing artifacts superimposed to the eye. For this, parallel transmit techniques using multi-channel TX/RX coil arrays might be productively employed for spatially selective excitation [46]. These techniques make us of exquisite control over the electromagnetic fields by modulating amplitude and phase used for excitation of each independent transmit channel. Potential applications include targeted or curved excitation and zoomed imaging using a FOV smaller than the object size [47]. Zonal imaging with tailored parallel transmit pulses can be accomplished without the risk of aliasing artifacts

since magnetization is only excited in the target area, which has tremendous practical implications for future ophthalmic imaging applications.

It is a recognized limitation of this study that primarily low flip angle gradient echo imaging techniques were applied due to RF power deposition constraints. MR imaging techniques that encompass trains of RF refocusing pulses, e.g. fast spin-echo (FSE) techniques can easily reach and exceed the SAR limits at 7.0 T [48]. Further FSE improvements shall include the development of RF pulses that unlike conventional refocusing RF pulses are less sensitive to non-uniformities in the transmission field of multi-channel surface coil arrays used for RF excitation at ultrahigh fields. Here, caution is warranted not to severely increase the minimum inter-echo time, which could be challenging if not elusive for rapid imaging. Also, the merits of parallel imaging strategies can be employed to address RF power deposition constraints, which otherwise would force a lengthening in the echo time and repetition time. The need for reducing the RF power deposition at ultrahigh fields accentuates the complementary advantage of parallel imaging since it has been predicted that field strengths larger than 5.0 T promise to reduce the noise amplification in parallel imaging [42, 43]. Further improvements in image quality/contrast can be achieved by tailoring pulse sequences established for eye imaging at 1.5 T [26] and 3.0 T [27] for 7.0 T. To this end it is of essence to further reduce artifacts induced by susceptibility gradients or by eye motion. Here the proposed open RF coil design provides space for an eye-tracking and gaze fixation system to monitor eye position during data acquisition; an approach which would be beneficial to correct for eye motion induced motion artifacts. Taking the SNR gain at 7.0 T into account we also anticipate to expand our studies to diffusion-weighted imaging which might be helpful to differentiate ocular tumors from retinal detachment as suggested by a recent study at 1.5 T [49].

Progress in ophthalmic MRI at 7.0 T may serve to enhance the capabilities of MR image based biometry with the ultimate goal to support advanced intraocular lens implantation or refilling procedures that restore visual function and accommodation. Arguably, the notion that intraocular lenses are a contra-indication *per se* at 7.0 T is somewhat premature. However, gaining a better insight into the MR safety of intraocular lenses is of profound

relevance for ophthalmic MR developments at 7.0 T and their transfer into clinical practice due to an increasing patient population with a history of cataract surgery with intraocular lens implantation [50]. To this end it should be noted that recent phantom studies demonstrated that MRI at 7.0 T did not induce movement or RF heating of any of the investigated intraocular lenses [51]. Hence the authors concluded that all the tested intraocular lenses are considered safe for MRI up to and including 7 Tesla [51].

To conclude, we have shown that the proposed 6 channel transceiver coil has the capability to acquire high contrast, high spatial resolution images of the eye at 7.0 T. The RF penetration seems sufficient for healthy subjects and patients. $B_1^+$ non-uniformities can be mitigated with appropriate $B_1^+$ phase settings. The results underline the challenges of ocular imaging at 7.0 T and demonstrate that these issues can be offset by using tailored RF coil hardware. The benefits of such improvements would be in positive alignment with the needs of explorations that are designed to examine the potential of ultrahigh field MRI for the assessment of spatial arrangements of the eye segments and their masses with the ultimate goal to provide guidance during diagnostic assessment and treatment of ophthalmological diseases.

## References

1. Mafee MF, Karimi A, Shah J, et al. Anatomy and pathology of the eye: role of MR imaging and CT. Neuroimaging Clin N Am. 2005;15:23-47.

2. Strenk SA, Strenk LM, Guo S. Magnetic resonance imaging of aging, accommodating, phakic, and pseudophakic ciliary muscle diameters. J Cataract Refract Surg. 2006;32:1792-8.

3. Bolacchi F, Garaci FG, Martucci A, et al. Differences between proximal versus distal intraorbital optic nerve diffusion tensor magnetic resonance imaging properties in glaucoma patients. Invest Ophthalmol Vis Sci. 2012;53:4191-6.

4. Zhang Y, San Emeterio Nateras O, Peng Q, et al. Blood flow MRI of the human retina/choroid during rest and isometric exercise. Invest Ophthalmol Vis Sci. 2012;53:4299-305.

5. Sepahdari AR, Kapur R, Aakalu VK, et al. Diffusion-weighted imaging of malignant ocular masses: initial results and directions for further study. AJNR Am J Neuroradiol. 2012;33:314-9.

6. Zhang Y, Nateras OS, Peng Q, et al. Lamina-specific anatomic magnetic resonance imaging of the human retina. Invest Ophthalmol Vis Sci. 2011;52:7232-7.

7. Bert RJ, Patz S, Ossiani M, et al. High-resolution MR imaging of the human eye 2005. Acad Radiol. 2006;13:368-78.

8. Malhotra A, Minja FJ, Crum A, et al. Ocular anatomy and cross-sectional imaging of the eye. Semin Ultrasound CT MR. 2011;32:2-13.

9. Apushkin MA, Shapiro MJ, Mafee MF. Retinoblastoma and simulating lesions: role of imaging. Neuroimaging Clin N Am. 2005;15:49-67.

10. Pineles SL, Demer JL, Holland GN, et al. External ophthalmoplegia in human immunodeficiency virus-infected patients receiving antiretroviral therapy. J AAPOS. 2012;16:529-33.

11. Papadopoulou D, Moulin AP, Zografos L, et al. How would you manage this small melanocytic choroidal tumour? Small choroidal melanoma hiding a large extrascleral extension. Br J Ophthalmol. 2012;96:1530, 9-40.

12. Clark RA, Rosenbaum AL, Demer JL. Magnetic resonance imaging after surgical transposition defines the anteroposterior location of the rectus muscle pulleys. J AAPOS. 1999;3:9-14.

13. Weir RE, Evans S, Hajdu SD, et al. The convex retina: optical coherence tomography in hypermetropic shift, without choroidal folds, from intraconal cavernous haemangioma. Orbit. 2009;28:398-400.

14. Brisse HJ, Guesmi M, Aerts I, et al. Relevance of CT and MRI in retinoblastoma for the diagnosis of postlaminar invasion with normal-size optic nerve: a retrospective study of 150 patients with histological comparison. Pediatr Radiol. 2007;37:649-56.

15. Tourbah A. Contribution of imaging to the diagnosis of optic neuropathies. Rev Neurol (Paris). 2012;168:702-5.

16. Khanna S, Sharma A, Huecker J, et al. Magnetic resonance imaging of optic neuritis in patients with neuromyelitis optica versus multiple sclerosis. J Neuroophthalmol. 2012;32:216-20.

17. Platnick J, Crum AV, Soohoo S, et al. The globe: infection, inflammation, and systemic disease. Semin Ultrasound CT MR. 2011;32:38-50.

18. de Graaf P, Barkhof F, Moll AC, et al. Retinoblastoma: MR imaging parameters in detection of tumor extent. Radiology. 2005;235:197-207.

19. de Graaf P, Pouwels PJ, Rodjan F, et al. Single-shot turbo spin-echo diffusion-weighted imaging for retinoblastoma: initial experience. AJNR Am J Neuroradiol. 2012;33:110-8.

20. de Graaf P, Goricke S, Rodjan F, et al. Guidelines for imaging retinoblastoma: imaging principles and MRI standardization. Pediatr Radiol. 2012;42:2-14.

21. Krueger PC, Stachs O, Hadlich S, et al. MR Microscopy of the Human Eye at 7.1 T and Correlation with Histopathology - Proof of Principle. Orbit. 2012;31:390-3.

22. Singh KD, Logan NS, Gilmartin B. Three-dimensional modeling of the human eye based on magnetic resonance imaging. Invest Ophthalmol Vis Sci. 2006;47:2272-9.

23. Stachs O, Langner S, Terwee T, et al. In vivo 7.1 T magnetic resonance imaging to assess the lens geometry in rabbit eyes 3 years after lens-refilling surgery. J Cataract Refract Surg. 2011;37:749-57.

24. Richdale K, Sinnott LT, Bullimore MA, et al. Quantification of Age-Related and per Diopter Accommodative Changes of the Lens and Ciliary Muscle in the Emmetropic Human Eye. Invest Ophthalmol Vis Sci. 2013.

25. Jones CE, Atchison DA, Meder R, et al. Refractive index distribution and optical properties of the isolated human lens measured using magnetic resonance imaging (MRI). Vision Res. 2005;45:2352-66.

26. Patz S, Bert RJ, Frederick E, et al. T(1) and T(2) measurements of the fine structures of the in vivo and enucleated human eye. J Magn Reson Imaging. 2007;26:510-8.

27. Mafee MF, Rapoport M, Karimi A, et al. Orbital and ocular imaging using 3- and 1.5-T MR imaging systems. Neuroimaging Clin N Am. 2005;15:1-21.

28. Richdale K, Wassenaar P, Teal Bluestein K, et al. 7 Tesla MR imaging of the human eye in vivo. J Magn Reson Imaging. 2009;30:924-32.

29. Lopez MA, Ehses P, Breuer FA, et al. A Four-Channel Hole-Slotted Phased Array at 7 Tesla. Concepts in Magnetic Resonance Part B-Magnetic Resonance Engineering. 2010;37B:226-36.

30. Christ A, Kainz W, Hahn EG, et al. The Virtual Family—development of surface-based anatomical models of two adults and two children for dosimetric simulations. Physics in medicine and biology. 2010;55:N23.

31. Kozlov M, Turner R. Fast MRI coil analysis based on 3-D electromagnetic and RF circuit co-simulation. Journal of Magnetic Resonance. 2009;200:147-52.

32. IEC. 60601-2-33 Medical electrical equipment - Part 2-33: Particular requirements for the basic safety and essential performance of magnetic resonance equipment for medical diagnosis. 3.0 ed; 2010.

33. Santoro D, Rivoire J, Meise F, et al. Three-dimensional mapping of the B1 field using an optimized phase-based method: application to hyperpolarized 3He in lungs. Magn Reson Med. 2011;65:1166-72.

34. Carinci F, Santoro D, von Samson-Himmelstjerna F, et al. Characterization of phase-based methods used for transmission field uniformity mapping: a magnetic resonance study at 3.0 T and 7.0 T. PLoS One. 2013;8:e57982.

35. Schneider E, Glover G. Rapid in vivo proton shimming. Magn Reson Med. 1991;18:335-47.

36. Berkowitz BA, McDonald C, Ito Y, et al. Measuring the human retinal oxygenation response to a hyperoxic challenge using MRI: eliminating blinking artifacts and demonstrating proof of concept. Magn Reson Med. 2001;46:412-6.

37. Kellman P, McVeigh ER. Image reconstruction in SNR units: a general method for SNR measurement. Magn Reson Med. 2005;54:1439-47.

38. Wuerfel J, Sinnecker T, Ringelstein EB, et al. Lesion morphology at 7 Tesla MRI differentiates Susac syndrome from multiple sclerosis. Mult Scler. 2012;18:1592-9.

39. Sinnecker T, Dorr J, Pfueller CF, et al. Distinct lesion morphology at 7-T MRI differentiates neuromyelitis optica from multiple sclerosis. Neurology. 2012;79:708-14.

40. Khurana A, Eisenhut CA, Wan W, et al. Comparison of the diagnostic value of MR imaging and ophthalmoscopy for the staging of retinoblastoma. Eur Radiol. 2013;23:1271-80.

41. Weiger M, Pruessmann KP, Boesiger P. 2D SENSE for faster 3D MRI. Magnetic Resonance Materials in Physics, Biology and Medicine. 2002;14:10-9.

42. Ohliger MA, Grant AK, Sodickson DK. Ultimate intrinsic signal-to-noise ratio for parallel MRI: electromagnetic field considerations. Magn Reson Med. 2003;50:1018-30.

43. Wiesinger F, Boesiger P, Pruessmann KP. Electrodynamics and ultimate SNR in parallel MR imaging. Magn Reson Med. 2004;52:376-90.

44. Niendorf T, Sodickson DK. Highly accelerated cardiovascular magnetic resonance imaging: concepts and clinical applications. Conf Proc IEEE Eng Med Biol Soc. 2006;1:373-6.

45. Niendorf T, Sodickson DK. Parallel imaging in cardiovascular MRI: methods and applications. NMR Biomed. 2006;19:325-41.

46. Schneider JT, Kalayciyan R, Haas M, et al. Inner-volume imaging in vivo using three-dimensional parallel spatially selective excitation. Magn Reson Med. 2012.

47. Zelinski AC, Angelone LM, Goyal VK, et al. Specific absorption rate studies of the parallel transmission of inner-volume excitations at 7T. J Magn Reson Imaging. 2008;28:1005-18.

48. Utting JF, Kozerke S, Luechinger R, et al. Feasibility of k-t BLAST for BOLD fMRI with a spin-echo based acquisition at 3 T and 7 T. Invest Radiol. 2009;44:495-502.

49. Erb-Eigner K, Willerding G, Taupitz M, et al. Diffusion-Weighted Imaging of Ocular Melanoma. Invest Radiol. 2013.

50. Erie JC, Baratz KH, Hodge DO, et al. Incidence of cataract surgery from 1980 through 2004: 25-year population-based study. J Cataract Refract Surg. 2007;33:1273-7.

51. van Rijn GA, Mourik JE, Teeuwisse WM, et al. Magnetic resonance compatibility of intraocular lenses measured at 7 Tesla. Invest Ophthalmol Vis Sci. 2012;53:3449-53.

## Figure Captions

**Figure 1:**

**a)** Schematic drawing of the coil array depicting the basic coil design, illustrating the angulation of the elements and identifying the individual elements. **b)** Basic circuit diagram of the 6-channel coil array superimposed to a virtual head of the voxel model "Duke" used for EMF simulations. Coil elements are depicted in yellow. **c)** The conductor layout and its dimensions. The decoupling of the next neighboring elements is illustrated by two coaxial cables and two capacitive trimmers in between.

**Figure 2:**

**left)** Photograph of the 6 channel TX/RX array tailored for ocular imaging showing the cable traps, conductors and cabling together with the coil casing and a mirror which allows for fixating a point in the isocenter of the scanner bore. **right)** Phantom setup with the RF coil placed on a cylindrical phantom used for the validation of the EMF simulations.

**Figure 3:**

S-parameter matrix **(a)** with standard deviation **(b)** averaged over six volunteers. 6x6 noise correlation matrix derived from phantom measurements using the phantom **(c)** and averaged over six healthy subjects **(d)**.

**Figure 4:**

Schematic view of the element position with respect to the eyes of the human voxel model Duke **(a)**. Angles to the center of the right eye are 52° and 53°. Angles to the center of the left eye are 53° and 48°. $B_1^+$ distributions derived from numerical EMF simulations for a transversal slice through the eye using **(b)** the sum of square combination of the individual fields displaying a pixel wise constructive interference as the upper bound for any RF shimming, **(c)** a circular polarized phase setting (PS1) with respect to the loop plane normal, **(d)** a circular polarized phase setting (PS2) that is centered in the right eye and in the left eye and **(e)** the

$B_1^+$ optimized phase setting PS3. PS3 provided improvements in $B_1^+$ uniformity for regions covering the eyes versus PS2 as illustrated by the PS3-PS2 difference map **(f)**.

**Figure 5:**

$SAR_{10g}$ distribution derived from EMF simulations using the human voxel model "Ella" **(left)** and "Duke" **(right)** for the $B_1^+$ optimized phase setting PS3 employed in all *in vivo* experiments. A surface plot of the local $SAR_{10g}$ **(top row)** and a transverse slice **(bottom row)** covering the location of the global maximum of the local $SAR_{10g}$ are shown. By adjusting the positioning of the coil to a minimum distance of 12 mm to the head using the eyebrows and the cheekbones as anatomical references, the anatomy of the nose of the male voxel model is slightly more exposed to SAR. The global maximum of the local $SAR_{10g}$ obtained for PS3 did not exceed the 10 W/kg limit given by the IEC guidelines for an input power of 0.8 $W_{rms}$.

**Figure 6:**

Qualitative comparison of simulated $B_1^+$ distributions **(top)** and experimental normalized $B_1$+maps **(bottom)** obtained for all 6 coil channels. For $B_1^+$ mapping a cylindrical phantom was used in the numerical EMF simulations and in the experiments. For this purpose the phantom (radius=60 mm, length=250 mm) was setup with a tissue equivalent dielectric medium ($\varepsilon_r$ = 57.8, $\sigma$ = 0.78 S/m). For $B_1^+$ mapping a transmitter reference voltage of 50 Volt was used resulting in a nominal $B_1^+$=19.16 µT (normalized value=1). The $B_1^+$ maps derived from numerical simulations and experiments show a fair agreement.

**Figure 7:**

High spatial resolution (0.3 x 0.3 x 1.0 $mm)^3$ sagittal view of the human eye, which depict subtle anatomical details and which indicate rather uniform signal intensity. The image was derived from 3D gradient echo imaging **b)** Signal intensity profile through the lens and vitreous humor as depicted in **a)**. Across the short axis (red graph) of the lens a 7% change in signal intensity was observed. Along a line (red graph) connecting the center of the lens with the retina a signal intensity change of 15% was obtained from the vitreous humor. For a profile

perpendicular to the line connecting the lens (blue graph) with the retina a signal intensity change of 2% was determined. Signal intensity histogram obtained for the lens **(c)** and for the vitreous humor **(d)**.

**Figure 8:**

Transversal views of the eye derived from 3D gradient echo imaging using a spatial resolution of **a)** (0.2 x 0.2 x 1.0 mm)$^3$ and **b)** (0.3 x 0.3 x 1.0 mm)$^3$ together with sagittal views of the eye derived from **c)** inversion recovery prepared 3D gradient echo imaging using a spatial resolution of (0.4 x 0.4 x 1.0 mm)$^3$ and from **d)** $T_2$-weighted 2D fast spin-echo imaging with a spatial resolution of (0.25 x 0.25 x 0.7 mm)$^3$.

**Figure 9:**

Comparison of results derived from $T_2$-weighted 2D fast spin-echo imaging of healthy subjects using the TX1RX24 **(a,e)**, TX1RX1 **(b,f)**, TX1RX32 **(c,g)** head coil configuration versus the 6 channel TX/RX local array **(d,h)**. For the 6 channel TX/RX coil rather uniform signal intensity was observed across the eye **(m)**. Unlike the 6 channel TX/RX coil the TX1RX24, TX1RX1 and TX1RX32 head coil configurations yielded a substantial change in signal intensity across the eye **(l,k,l)**. For a profile (marked by the blue dotted line) perpendicular to the line connecting the lens with the retina (marked by the red dotted line) a mean signal intensity change of <5 % was determined for the 6 channel TX/RX array **(m)**. In comparison, the TX1R24 configuration showed a 90 % signal intensity decrease for the same profile **(i)**. When using the TX1RX1 configuration a mean signal intensity change of approximately 55 % was observed for a profile perpendicular to the line connecting the lens with the retina **(k).** The TX1RX32 configuration yielded a mean signal intensity change of approximately 55 % for the same profile.

**Figure 10:**

Sagittal **(a)** and transversal **(b)** *in vivo* images of the right eye obtained from 3D gradient echo imaging (spatial resolution (0.3 x 0.3 x 1.0) mm$^3$) of a patient suffering from a malignant

melanoma of choroidea with retinal detachment. Spatial resolution was further improved to (0.2 x0.2 x 1.0) $mm^3$ for the transversal **(c)** view of the right eye of the same patient shown in **b)**. Total scan time was 3:12 min for **a)** and **b)** and 2:09 min for **c)**. Zoomed sagittal views of the left eye obtained from **d)** 3D gradient echo imaging (spatial resolution (0.3 x 0.3 x 1.0) $mm^3$ ) and from **e)** 2D $T_2$-weighted fast spin-echo imaging (spatial resolution (0.25 x 0.25 x 0.7) $mm^3$ ) of another patient suffering from a malignant melanoma of choroidea with retinal detachment.

.

Figure 1
Click here to download high resolution image

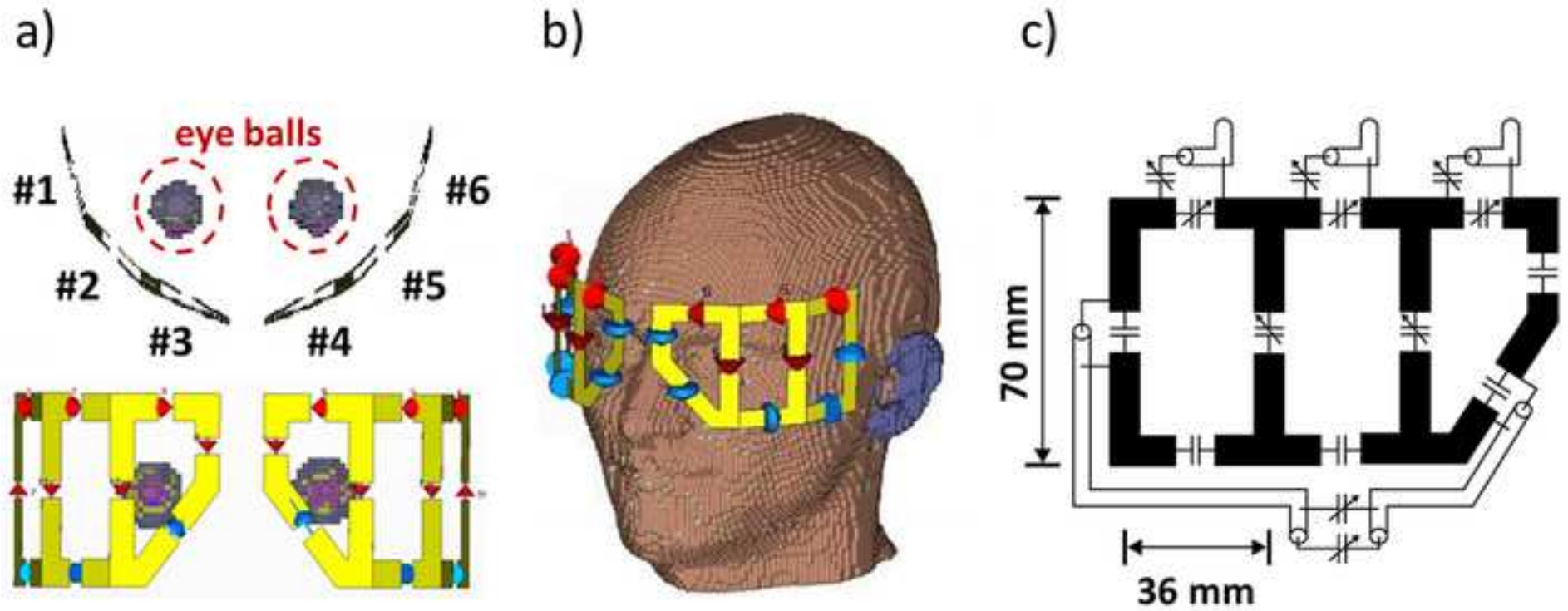

Figure 2
Click here to download high resolution image

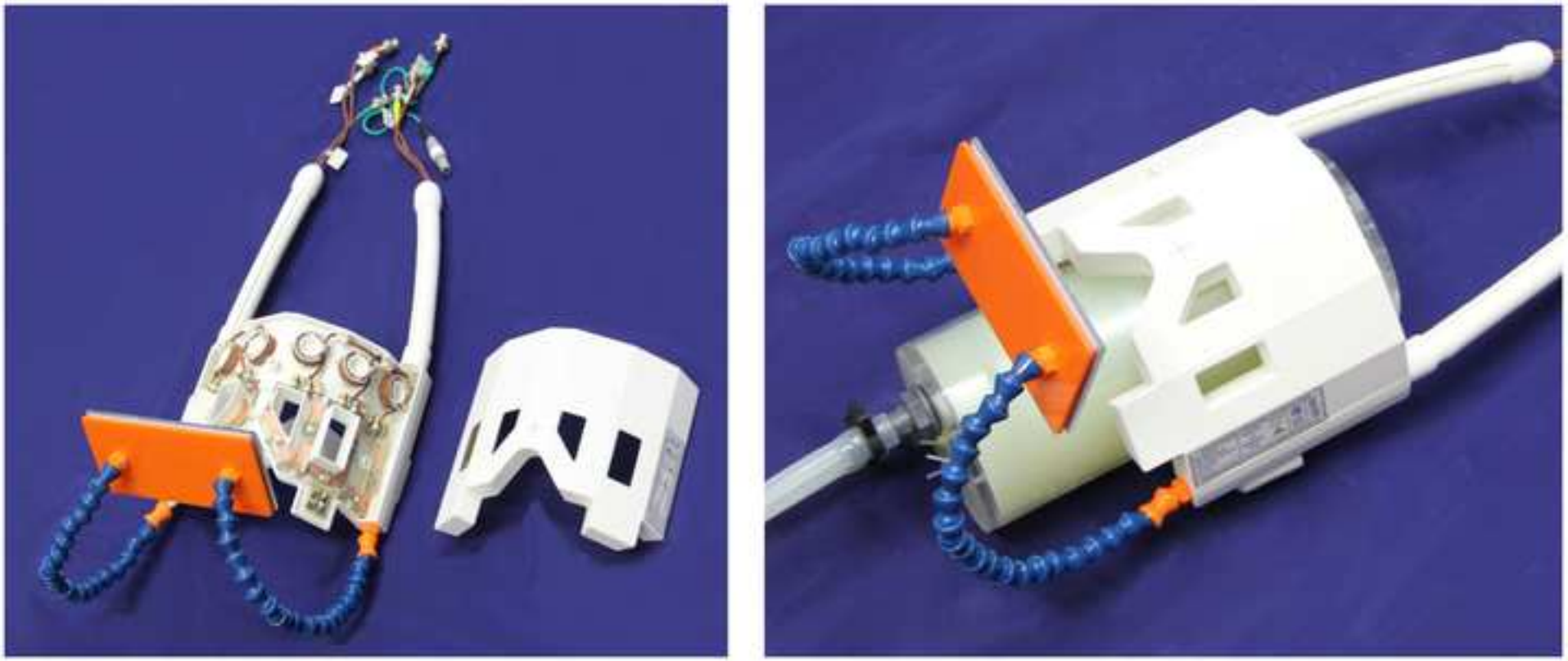

Figure 3
Click here to download high resolution image

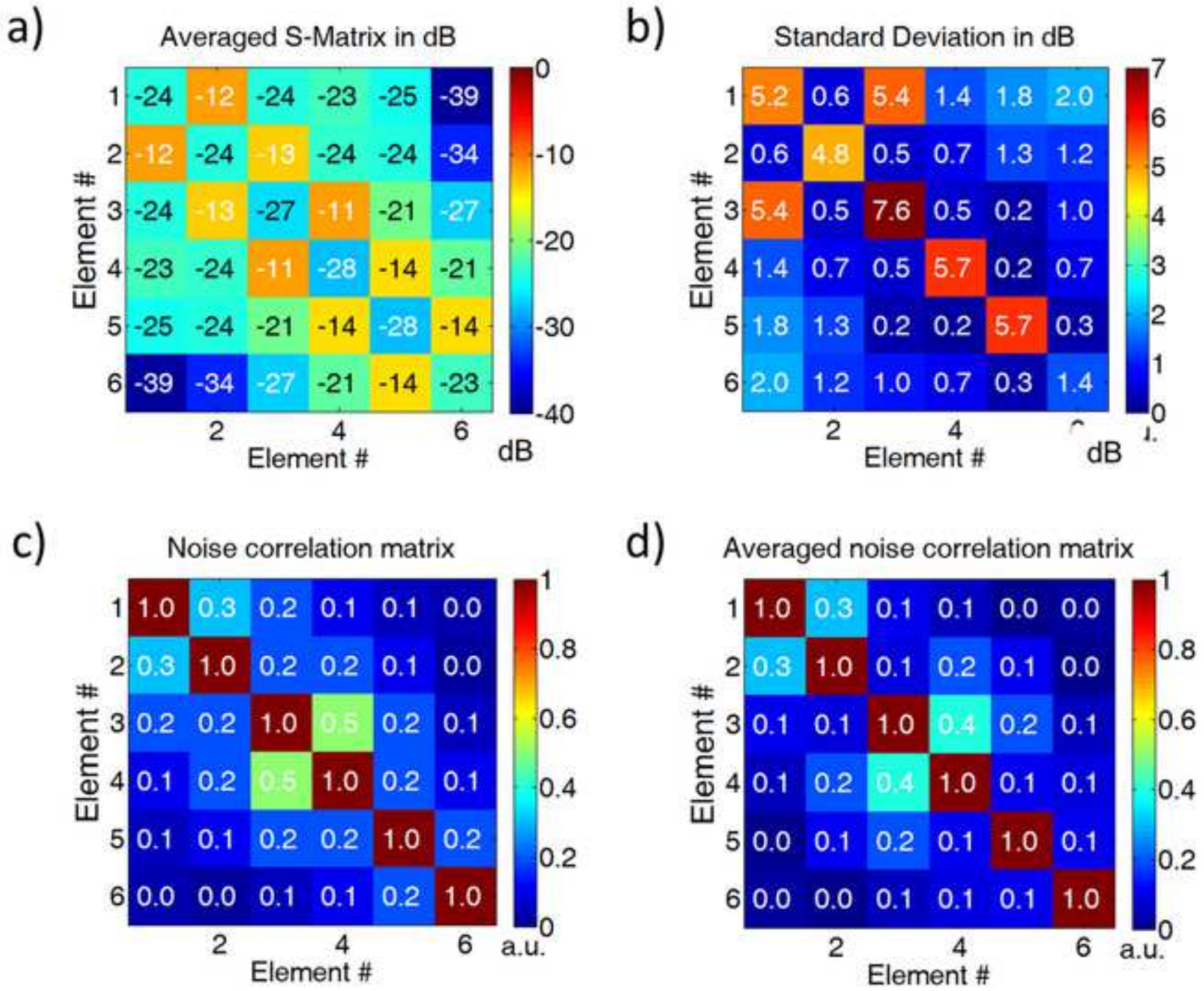

Figure 4
Click here to download high resolution image

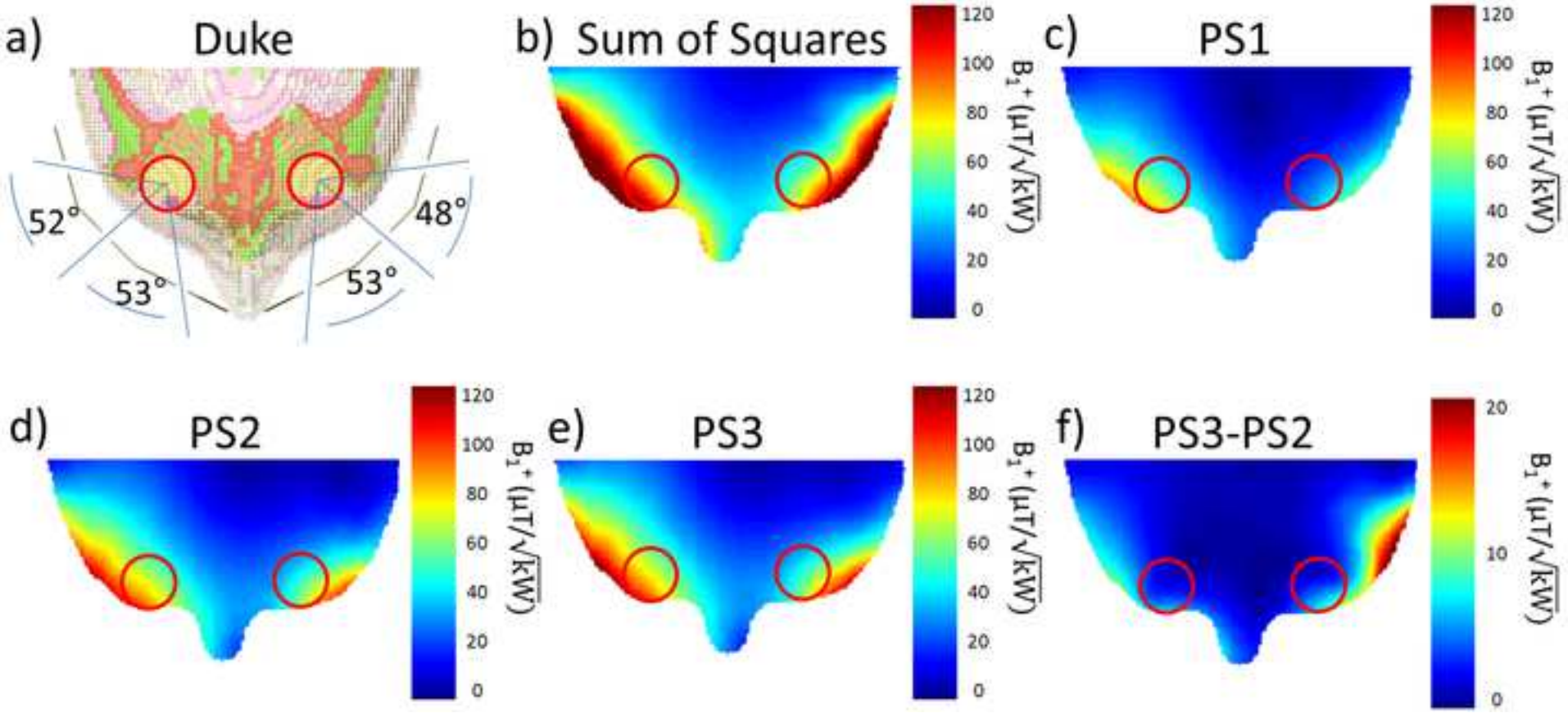

Figure 5
Click here to download high resolution image

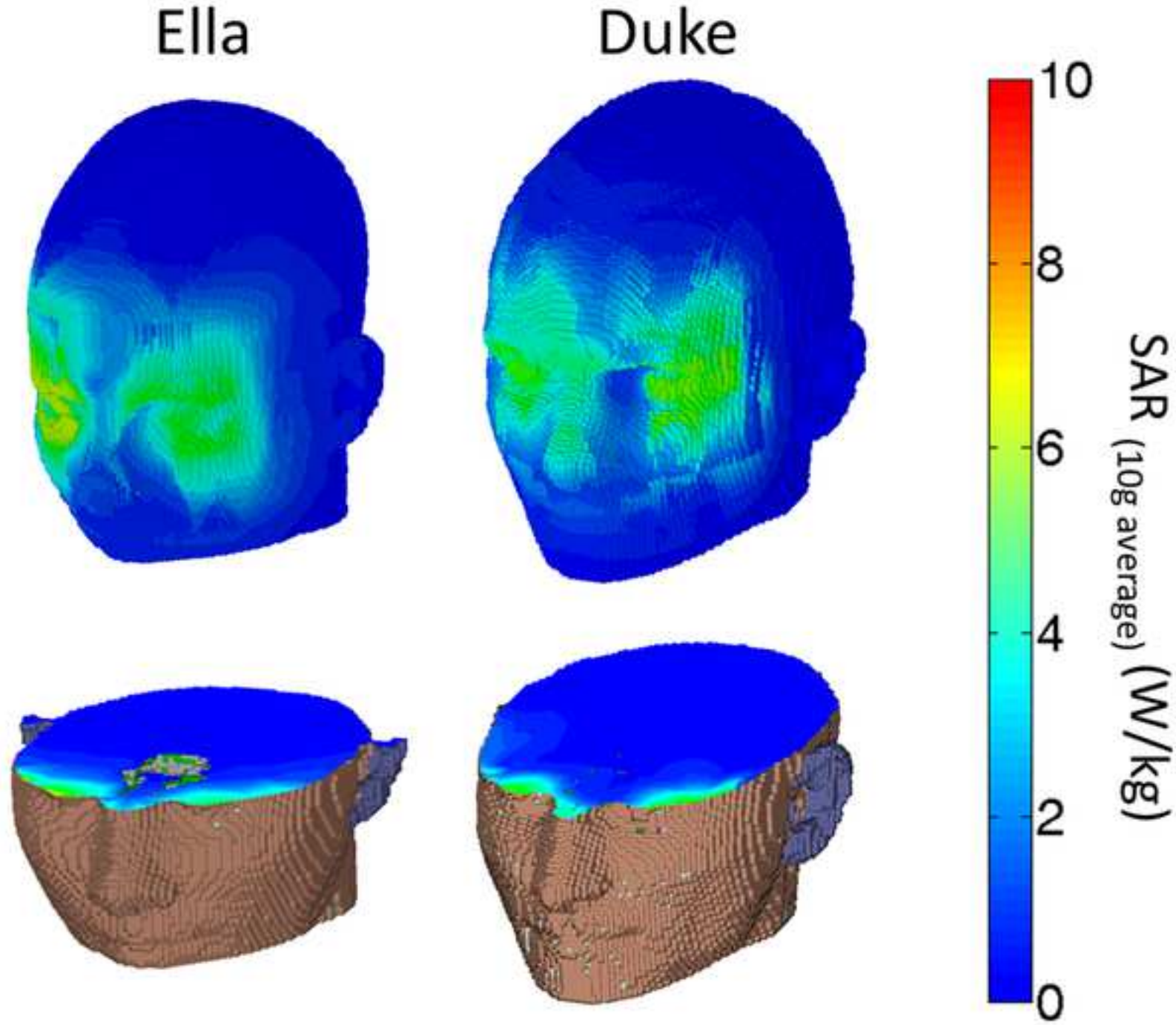

Figure 6
Click here to download high resolution image

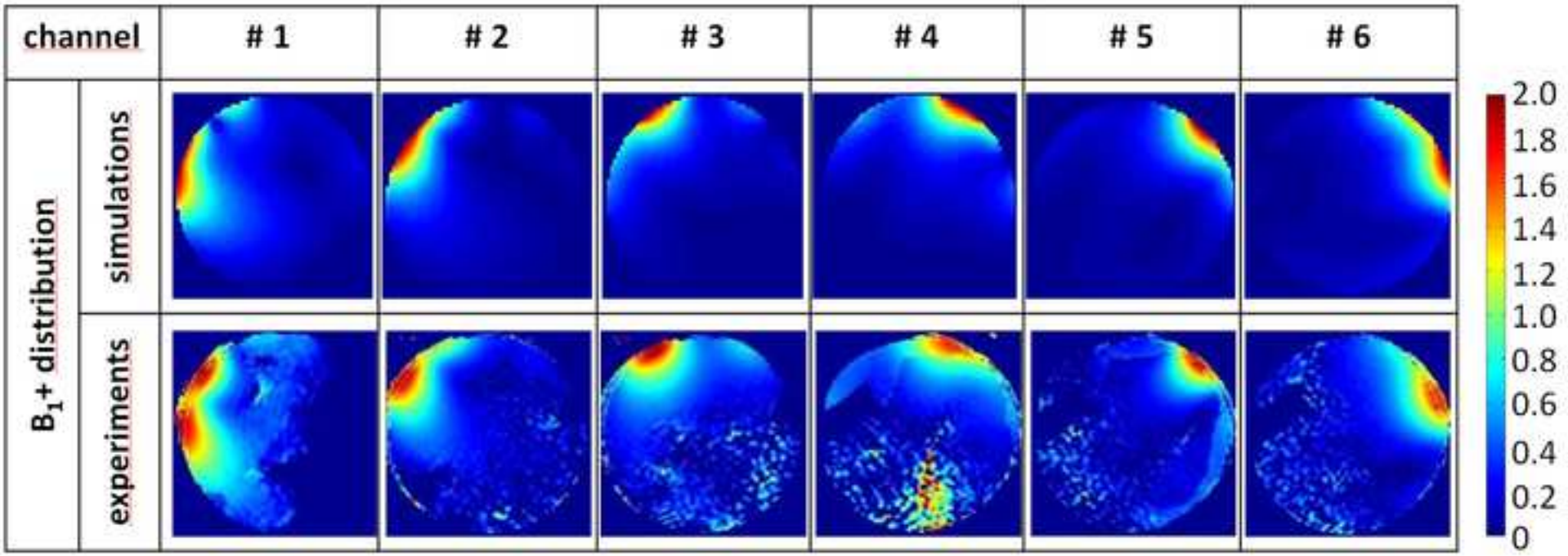

Figure 7
Click here to download high resolution image

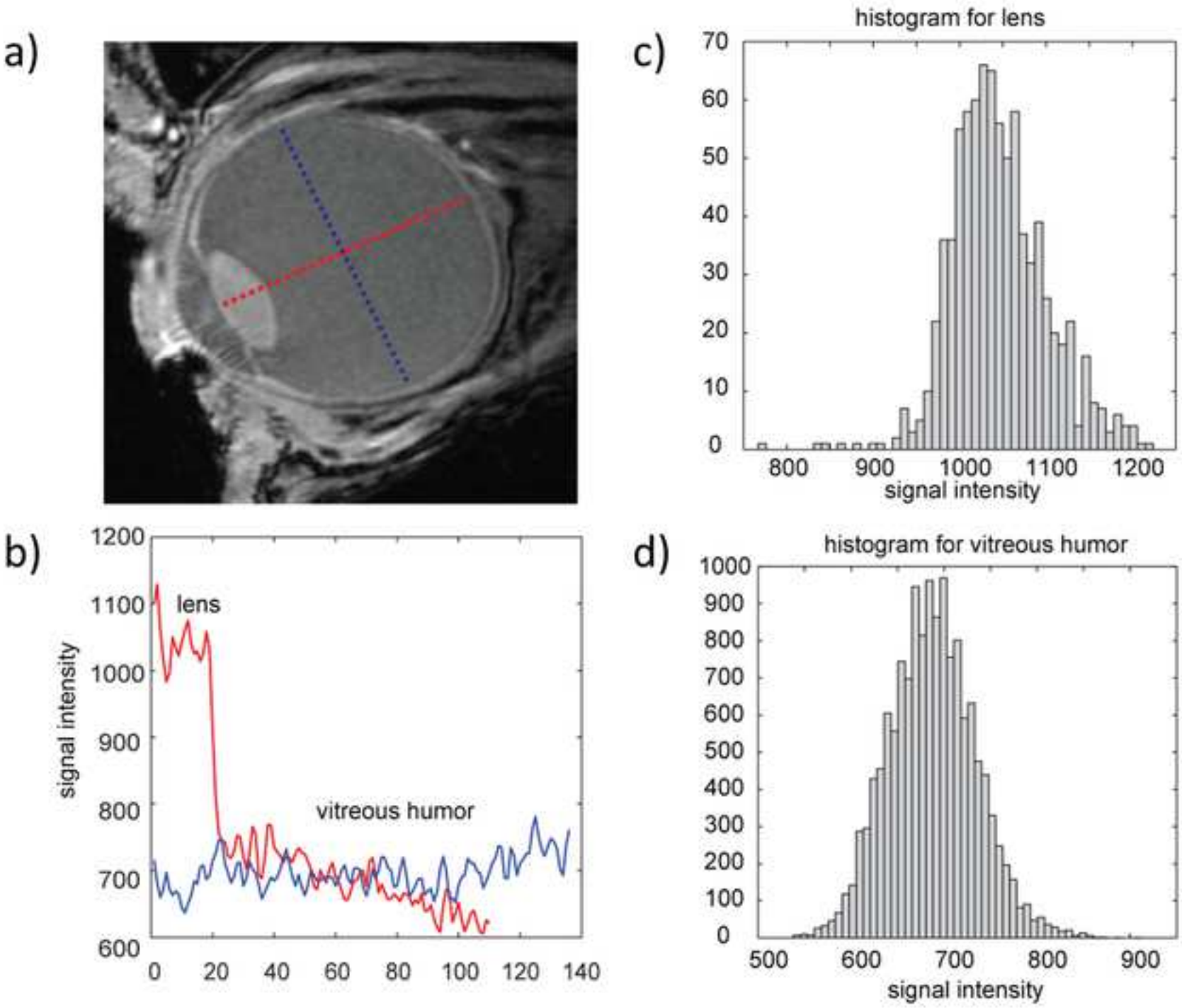

Figure 8
Click here to download high resolution image

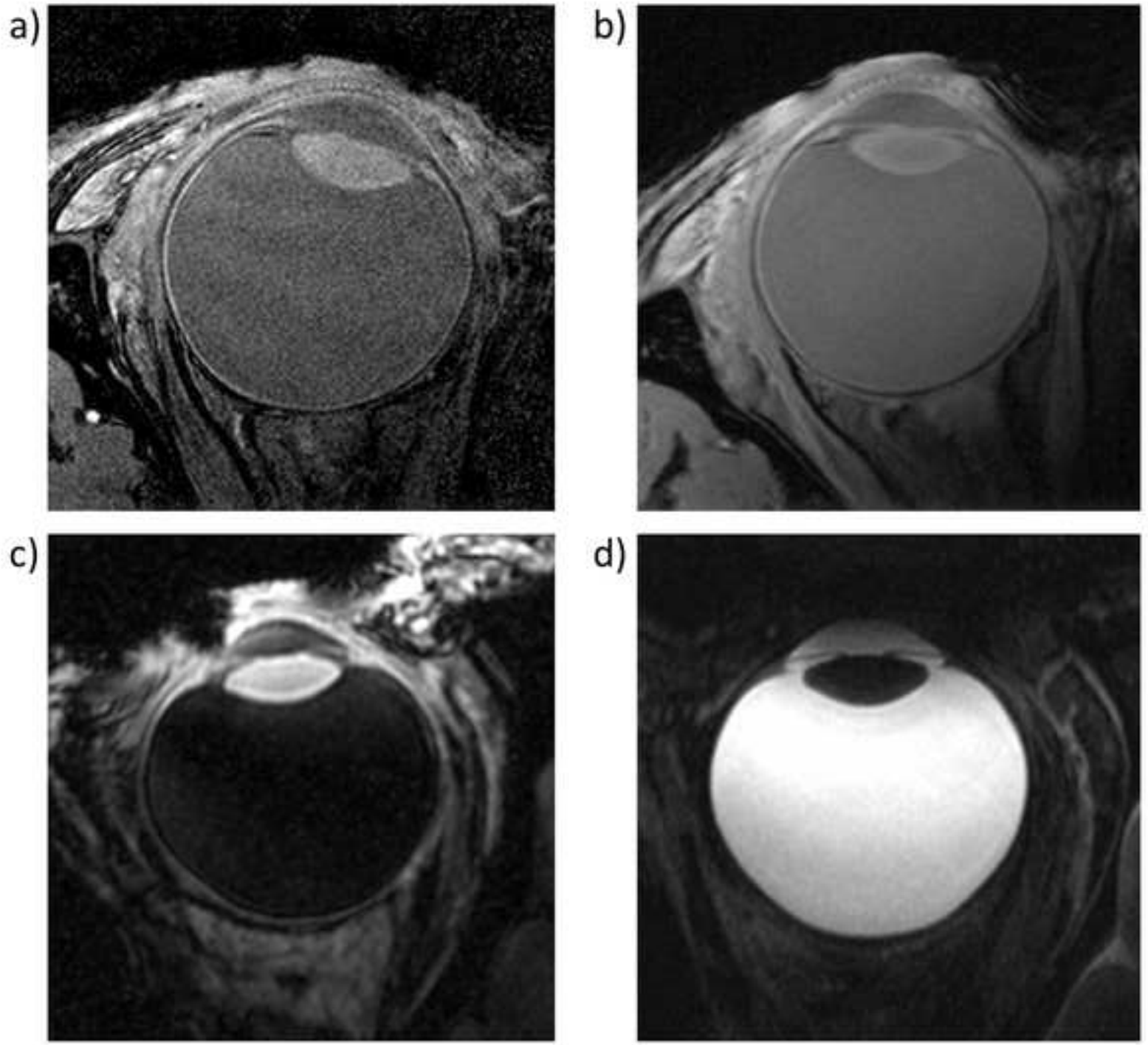

Figure 9
Click here to download high resolution image

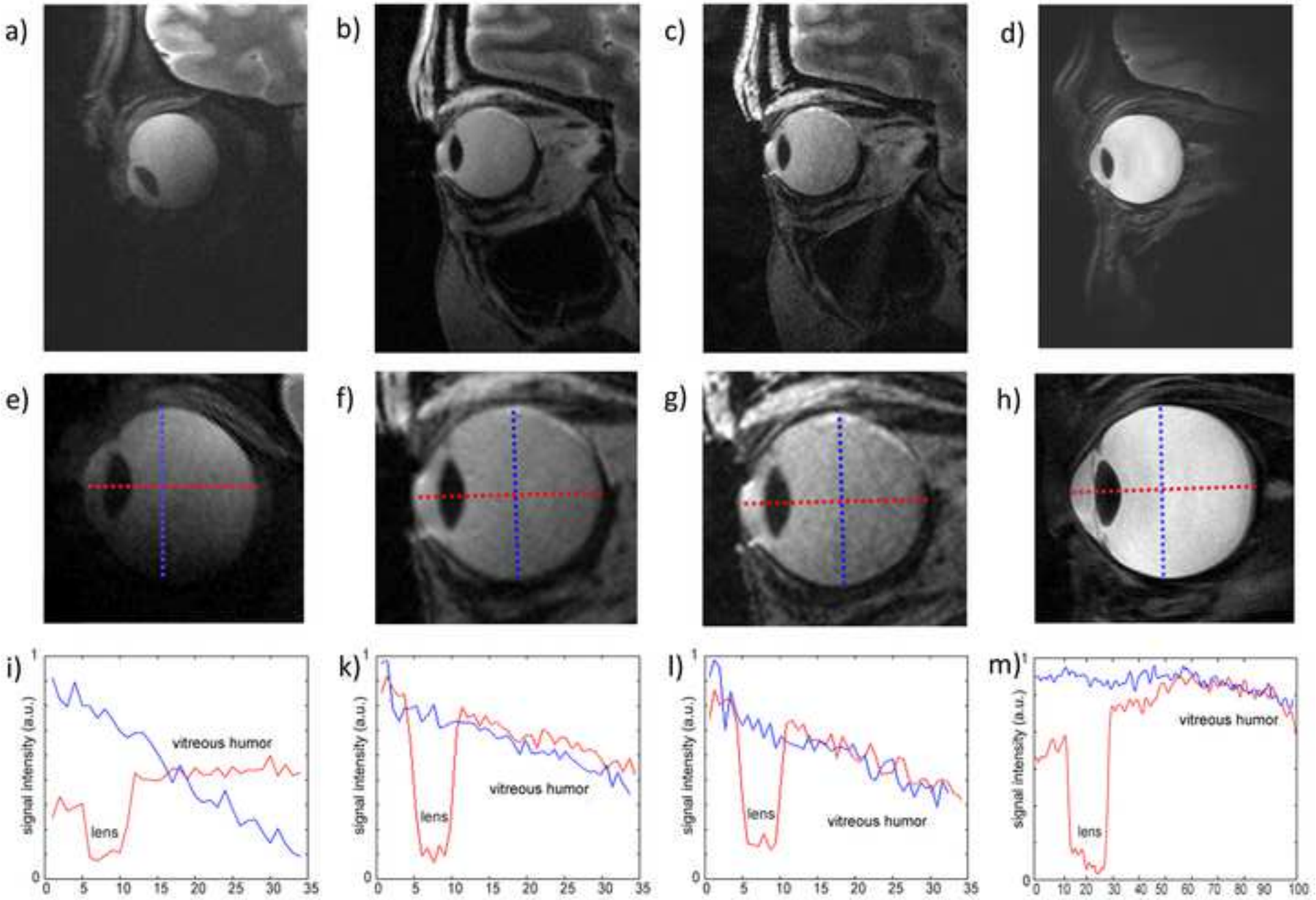

Figure 10
Click here to download high resolution image